communications physics

Article

https://doi.org/10.1038/s42005-024-01559-z

# Phonon-mediated temperature dependence of $Er^{3+}$ optical transitions in $Er_2O_3$



Adam Dodson [1] ✉, Hongrui Wu[1], Anuruddh Rai[2], Sohm Apte [2], Andrew O'Hara[1,3], Benjamin Lawrie [4,5], Yongqiang Wang[6], Akira Ueda[7], Halina Krzyżanowska[1,8], Michael Titze [9], Jimmy Davidson[1], Anthony Hmelo[1], Agham B. Posadas[2], Alexander A. Demkov [2], Sokrates T. Pantelides [1,10], Leonard C. Feldman [1,11] & Norman H. Tolk[1]

Characterization of the atomic level processes that determine optical transitions in emerging materials is critical to the development of new platforms for classical and quantum networking. Such understanding often emerges from studies of the temperature dependence of the transitions. We report measurements of the temperature dependent $Er^{3+}$ photoluminescence in single crystal $Er_2O_3$ thin films epitaxially grown on Si(111) focused on transitions that involve the closely spaced Stark-split levels. Radiative intensities are compared to a model that includes relevant Stark-split states, single phonon-assisted excitations, and the well-established level population redistribution due to thermalization. This approach, applied to the individual Stark-split states and employing $Er_2O_3$ specific single-phonon-assisted excitations, gives good agreement with experiment. This model allows us to demonstrate the difference in the electron-phonon coupling of the $^4S_{3/2}$ and $^2H_{11/2}$ states of $Er^{3+}$ in $E_2O_3$ and suggests that the temperature dependence of $Er^{3+}$ emission intensity may vary significantly with small shifts in the wavelength (~0.1 nm) of the excitation source.

Rare-earth elements have applications in light phosphors, lasers, optical thermometry, telecom amplifiers, and emerging applications in quantum information science[1,2]. Among the rare-earth elements, erbium (Er) exhibits compelling properties, with luminescence in the telecom band originating from the well-known $^4I_{13/2} \rightarrow {}^4I_{15/2}$ transition that may serve as a resource for practical and scalable quantum networks[3,4]. The host material influences the erbium emission spectrum through interactions with the local environment, primarily the crystal field. This perturbation results in the closely spaced Stark-split levels of the $Er^{3+}$ ground and excited states as observed in the emission spectrum[5,6]. The temperature-dependent emission intensity is consequently influenced by thermally mixed Stark-split states and phonon-assisted excitations between the ground and excited states. For applications, where narrow bandwidths may be desirable, understanding of the off-resonance excitation between Stark-split states presents another design parameter for system optimization.

Photoluminescence from $Er^{3+}$ incorporated into a wide range of materials has been explored extensively[7–24]. In these studies, the various interactions of $Er^{3+}$ with its local environment, including phonon-assisted processes like anti-Stokes/Stokes excitation, energy transfer between rare-earth ions, and de-excitation of $Er^{3+}$ ions, were explored by examining the temperature dependence of $Er^{3+}$ photoluminescence. The temperature dependence of these processes was experimentally demonstrated and analytically described by Auzel[25].

One common finding in these works was that the $^2H_{11/2}$ and $^4S_{3/2}$ levels of $Er^{3+}$ are thermally coupled due to their close energy spacing[7,12,15,26]. It is also important to note that in those works involving anti-Stokes/Stokes excita-

[1]Department of Physics and Astronomy, Vanderbilt University, Nashville, TN 37235, USA. [2]Department of Physics, The University of Texas, Austin, TX 78712, USA. [3]Department of Physics, Western Michigan University, Kalamazoo, MI 49008, USA. [4]Materials Science and Technology Division, Oak Ridge National Laboratory, Oak Ridge, TN 37830, USA. [5]Oak Ridge National Laboratory, Center for Nanophase Materials Sciences, Oak Ridge, TN 37830, USA. [6]Materials Science and Technology Division, Los Alamos National Laboratory, Los Alamos, NM 87545, USA. [7]Department of Life and Physical Sciences, Fisk University, Nashville, TN 37208, USA. [8]Institute of Physics, Maria Curie-Sklodowska University, Pl. M. Curie-Sklodowskiej 1, 20-031 Lublin, Poland. [9]Sandia National Laboratories, Albuquerque, NM 87123, USA. [10]Department of Electrical and Computer Engineering, Vanderbilt University, Nashville, TN 37235, USA. [11]Department of Physics and Astronomy, Rutgers University, Piscataway, NJ 08901, USA. ✉e-mail: adam.d.dodson@vanderbilt.edu

tion, modeling the observed photoluminescence often invoked an effective phonon energy associated with the excitation process[14,15,22,25]. Further, the modeling of the temperature dependence only considered transitions among the main energy levels labeled as the $^{2S+1}L_j$ states of $Er^{3+}$ (Fig. 1a), rather than transitions between the individual Stark-split levels of those $^{2S+1}L_j$ states.

For the specific case of the temperature-dependent photoluminescence of $Er^{3+}$ in $Er_2O_3$, the literature is more scarce and a majority focuses on the temperature dependence of photoluminescence arising from the $^4I_{13/2} \rightarrow {}^4I_{15/2}$ transition[14,16,21,24]. In the work by Omi et al.[14], abnormal temperature dependence of the photoluminescence arising from the $^4I_{13/2} \rightarrow {}^4I_{15/2}$ was observed when exciting $Er^{3+}$ with a laser at 532 nm. This behavior was attributed to $Er^{3+}$ in the $^4I_{15/2}$ state being excited to the $^2H_{11/2}$ via an anti-Stokes single-phonon-assisted excitation. In line with the literature cited above, the excitation was modeled to occur between the $^{2S+1}L_j$ states of $Er^{3+}$ and invoked effective phonon energy.

Here, we extend the existing work by reporting detailed measurements of the temperature-dependent photoluminescence intensity from 4 to 300 K which arise from individual Stark–Stark transitions in the $^4S_{3/2} \rightarrow {}^4I_{15/2}$, $^4S_{3/2} \rightarrow {}^4I_{13/2}$, and $^2H_{11/2} \rightarrow {}^4I_{15/2}$ transition manifolds of $Er^{3+}$ in $Er_2O_3$ induced by an off-resonance narrowband CW laser operating at 532 nm, a common excitation source in many photoluminescence setups. Isolating the individual Stark–Stark transitions from the transitions manifolds allows us to reveal more subtle distinctions in the excitation mechanism, particularly at low temperatures. The samples were epitaxial single crystal $Er_2O_3$ grown on Si(111)-oriented face. This choice of samples ensured that each emitting $Er^{3+}$ uniformly experienced the same crystal field and hence the same Stark-split level spectrum. This condition may not be fulfilled in implanted samples, defective/non-crystalline samples, or even other Er-doped crystalline oxides. Critical to this study is that the incident radiation at 532 nm is not resonant with any level separation of $Er^{3+}$ ions in the $Er_2O_3$ system, motivating the study of the electron–phonon interactions of $Er^{3+}$ in $Er_2O_3$.

A modeling approach is introduced that invokes the individual $(j + ½)$ Stark-split levels within each $^{2S+1}L_j$ state and includes the appropriate laser-induced Stokes or anti-Stokes transitions between the Stark-split levels in the ground state $^4I_{15/2}$ and the Stark-split excited states of $^4S_{3/2}$ and $^2H_{11/2}$. This model, which gives good agreement with the experiment, shows that the temperature dependence of the observed photoluminescence from the individual Stark-split levels is a result of three distinct temperature-dependent processes: thermalization, anti-Stokes/Stokes excitation, and variations in the excited state lifetime due to thermal coupling of levels with disparate lifetimes. Most importantly, the population of emitting Stark-split states by non-resonant incoming radiation is enabled by specific single-phonon-assisted Stokes and anti-Stokes excitations which are enabled by the energy and bandwidth specific to phonons in cubic $Er_2O_3$. With this model, we are also able to show a difference in the strength of the electron-phonon coupling between $Er^{3+}$ ions in the $^4S_{3/2}$ and $^2H_{11/2}$ levels and suggest that the temperature-dependent emission from $Er^{3+}$ ions may vary significantly with small shifts in the wavelength (~0.1 nm) of the excitation source.

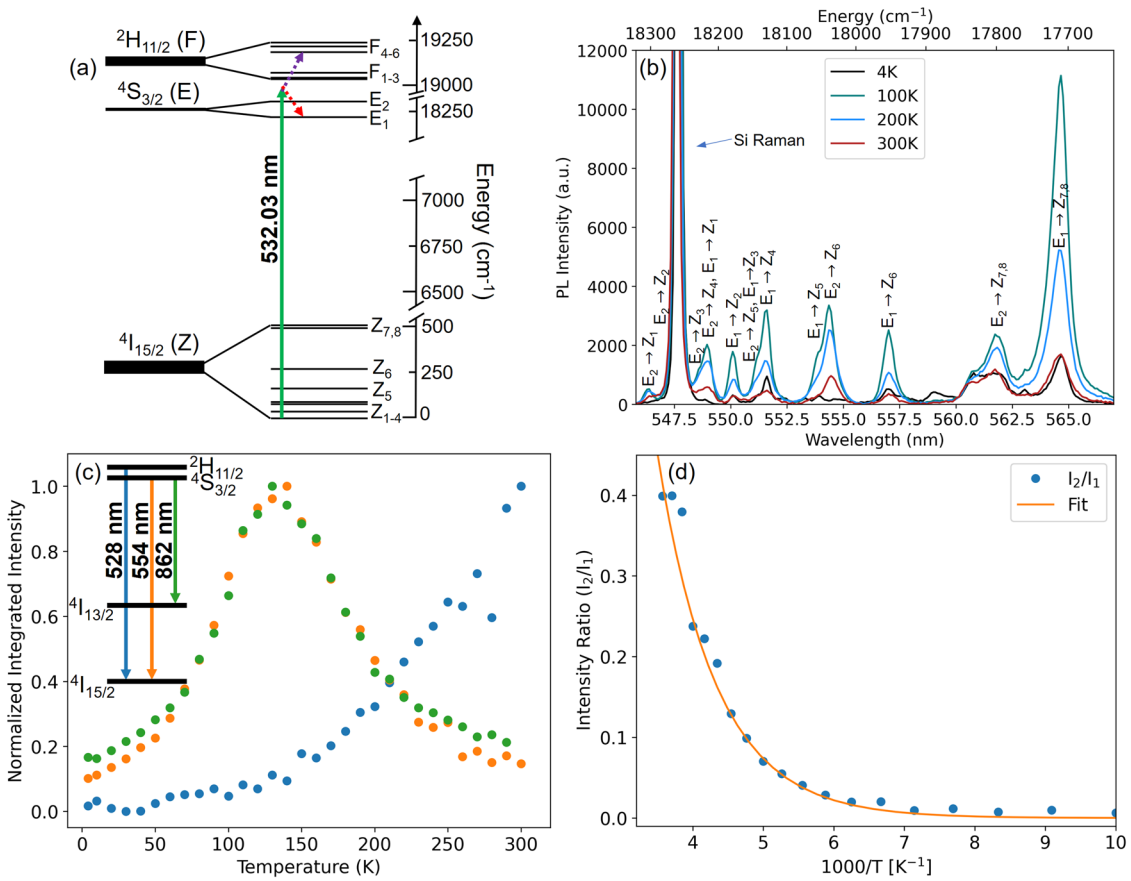


**Fig. 1 | Overview of observed $Er^{3+}$ temperature-dependent photoluminescence in $Er_2O_3$.** **a** Level diagram showing the doubly degenerate Stark-split levels of $^2H_{11/2}$,$^4S_{3/2}$, and $^4I_{15/2}$ of $Er^{3+}$ in $Er_2O_3$. Multiple subscripts in the labeling scheme are due to close spacing on the diagram. For instance, $Z_1$, $Z_2$, $Z_3$, and $Z_4$ are distinct, albeit closely spaced levels, and have to be labeled $Z_{1-4}$. Examples of Stokes (red dashed arrow) and anti-Stokes (purple dashed arrow) using a 532 nm laser (green solid line) are also shown. **b** $Er^{3+}$ photoluminescence from the $^4S_{3/2} \rightarrow {}^4I_{15/2}$ transition manifold in $Er_2O_3$ at several different temperatures. A Si Raman line from the Si substrate is noted at 547.7 nm. **c** Normalized integrated photoluminescence from the three transitions shown in the inset. The inset shows the relevant level diagram with the center of mass wavelengths indicated. The lines are included to guide the eyes. **d** Ratio of the integrated photoluminescence from $^2H_{11/2}$ and $^4S_{3/2}$. The fit line[26] is $A \exp\left(\frac{-E_{21}}{kT}\right)$, where $E_{21}$ is the energy spacing between the center of gravity[27] of the $^2H_{11/2}$ and $^4S_{3/2}$ levels. This demonstrates that the two levels are thermally coupled.

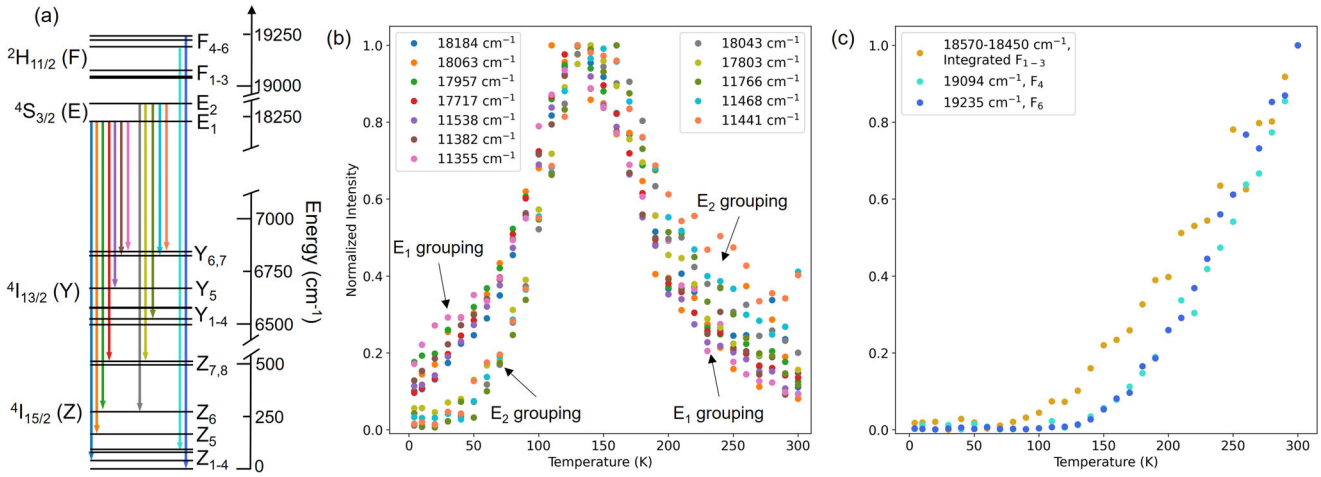


**Fig. 2 | Observed temperature dependence of photoluminescence from multiple Stark–Stark transitions of $Er^{3+}$ in $Er_2O_3$. a** $Er^{3+}$ level diagram showing the splitting of $^4S_{3/2}$,$^2H_{11/2}$,$^4I_{13/2}$ and $^4I_{15/2}$ due to the crystal field of $Er_2O_3$. Also shown are representative transitions. The transition lines are color-coded to the data shown in **b** and **c**. Normalized temperature-dependent intensity of peaks originating from several excited Stark-split levels in $^4S_{3/2}$ (**b**) and $^2H_{11/2}$ (**c**). Once normalized, the temperature-dependent behavior was identical for photoluminescence peaks originating from the same Stark-split level.

## Results

### Photoluminescence measurements

In the most common polytype of $Er_2O_3$, a body-centered cubic bixbyite structure, there are two symmetry sites for $Er^{3+}$, $C_2$, and $C_{3i}$. Of the 32 Er atoms in each unit cell, 8 Er sites have $C_{3i}$ symmetry, while the other 24 Er atoms have $C_2$ symmetry[24]. In $Er_2O_3$ the free ion $^{2S+1}L_j$ levels of $Er^{3+}$ are split by the crystal field into $j + 1/2$ Stark-split levels (Fig. 1a). This means that in $Er_2O_3$ a transition manifold $^{2S+1}L_j \rightarrow {}^{2S'+1}L'_{j'}$ will give rise to up to $(j + 1/2) \times (j'+1/2)$ total, often overlapping, spectral lines[27]. The crystal-field splitting and therefore the spectral lines will differ between symmetry sites. However, as the $C_{3i}$ site retains inversion symmetry electric dipole transitions are forbidden leaving only magnetically dipole-allowed transitions to occur. As a result, emission from this site has only been observed from the $^4I_{13/2} \rightarrow {}^4I_{15/2}$ transition manifold near 1550 nm[28]. The measurements described below detail photoluminescence from $Er^{3+}$ at the $C_2$ symmetry site of $Er_2O_3$. In Fig. 1b, there are 16 total lines present in the transition manifold $^4S_{3/2} \rightarrow {}^4I_{15/2}$, consistent with the spectral lines expected from $Er^{3+}$ at the $C_2$ symmetry site[27]. These lines are labeled with the initial and final Stark-split levels according to the scheme introduced by Gruber et al.[27] Individual lines from the other Stark–Stark transitions comprising the $^4S_{3/2} \rightarrow {}^4I_{13/2}$ and $^2H_{11/2} \rightarrow {}^4I_{15/2}$ transition manifolds can be similarly plotted (Supplementary Fig. 1) and labeled.

Figure 1c shows the temperature dependence of the normalized integrated intensity of the three transition manifolds shown in the inset $^4S_{3/2} \rightarrow {}^4I_{15/2}$, $^4S_{3/2} \rightarrow {}^4I_{13/2}$, and $^2H_{11/2} \rightarrow {}^4I_{15/2}$[27]. Although the measured absolute intensities of these lines vary over several orders of magnitude, it is convenient to normalize the integrated intensity when probing the temperature-dependent behaviors of the transition manifolds. The photoluminescence intensity arising from the radiative decay of closely spaced levels $^4S_{3/2}$ and $^2H_{11/2}$ to the ground state $^4I_{15/2}$ both display anomalous behavior in that neither decreases monotonically with increasing temperature as is typically observed in the photoluminescence of rare-earth ion transitions in other material systems[29]. Despite being thermally coupled (Fig. 1d), both manifolds display different temperature dependence. While the photoluminescence from $^2H_{11/2} \rightarrow {}^4I_{15/2}$ increases monotonically with temperature, the photoluminescence from $^4S_{3/2} \rightarrow {}^4I_{15/2}$ initially increases with temperature, peaking at around 140 K, and then decreases with temperature. Additionally, the measured temperature dependence of the photoluminescence arising from the $^4S_{3/2} \rightarrow {}^4I_{13/2}$ transition (green line in Fig. 1c), is similar to that of the photoluminescence arising from the $^4S_{3/2} \rightarrow {}^4I_{15/2}$ transition (orange line in Fig. 1c).

These observations suggest that the temperature dependence of the photoluminescence for a given transition depends almost entirely upon the initial excited state population, as the integrated photoluminescence originating from the $^4S_{3/2}$ level is observed to have the same temperature dependence regardless of the final state. This dependence becomes even more evident in the temperature dependence of the normalized intensity of transitions originating from individual Stark levels (Fig. 2a), particularly at lower temperatures. The normalized temperature dependence of the photoluminescence originating from the two Stark levels in $^4S_{3/2}$ is plotted in Fig. 2b. Despite the many different final Stark levels in both $^4I_{13/2}$ and $^4I_{15/2}$, there are two sets of curves grouped by originating Stark level, $E_1$ or $E_2$. This makes it clear that, at least for the $^4S_{3/2}$ levels, the normalized temperature dependence of the photoluminescence depends almost entirely on the excited state Stark level from which the $Er^{3+}$ ion decays.

Figure 2c shows the photoluminescence arising from the radiative decay of several different Stark levels in the $^2H_{11/2}$ state. Note that $F_{1-3}$ is the integrated intensity over photoluminescence arising from decays of all three Stark-split levels because the close spacing of the spectral lines prevents resolving the individual contributions. This again suggests that the normalized measured temperature dependence arises mainly from the originating Stark-level population. Resolution limitations along with the close spacing of the spectral lines from Stark–Stark transitions in the $^2H_{11/2} \rightarrow {}^4I_{15/2}$ manifold make a clearer determination difficult. However, it is also assumed here that the normalized temperature dependence of the photoluminescence from these levels depends almost entirely on the excited state Stark level. The data in Fig. 2b and c may be thought of as the "deconvolution" of the ensemble transitions shown in Fig. 1c. Such differences in temperature dependence (entire ensemble vs. individual Stark split states) may play a significant role in low-temperature applications.

It is well-known that the photon emission rate from an excited state is given by

$$I_i = A_i N_i, \tag{1}$$

where $A_i$ is the spontaneous emission rate ($A_i = \frac{1}{\tau_{i,r}}$ with $\tau_{i,r}$ as the radiative lifetime of the level $i$) and $N_i$ is the level population fraction. From the discussion above, we conclude that the dominant driver of the temperature dependence of the photoluminescence is the level population, $N_i$, of the decaying individual Stark level. In what follows, we develop a model to predict the temperature dependence of $N_i$ and by extension the observed photoluminescence arising from radiative decays from those levels.

### Theoretical modeling

Under the condition of steady-state excitation, the origin of the temperature dependence of $N_i$ can be attributed to the interplay of three distinct temperature-dependent processes. The first is the phonon-driven thermalization of $Er^{3+}$ ions between closely spaced Stark levels present in the excited states $^2H_{11/2}$ and $^4S_{3/2}$ as well as the ground state $^4I_{15/2}$. The second is the temperature dependence of the Stokes/anti-Stokes excitation cross sections, which permit Stark–Stark excitation between the ground and excited state. The third is the temperature-dependent excited state lifetime due to the thermal coupling of the excited state Stark levels of $^2H_{11/2}$ and $^4S_{3/2}$, which possess markedly different lifetimes. Below, we quantify these statements and develop an expression describing the full temperature dependence of $N_i$, which is reflected in the measured photoluminescence, over the range of 4 to 300 K.

The phonon-driven thermalization of $Er^{3+}$ ions amongst the closely spaced energy levels of $^2H_{11/2}$ and $^4S_{3/2}$, prior to radiative decay, is well-established[12,26]. Figure 1d confirms that in $Er_2O_3$, $Er^{3+}$ ions are thermalized between the $^2H_{11/2}$ and $^4S_{3/2}$ states prior to radiative decay. The energy separation between the lowest Stark level of $^2H_{11/2}$ and the highest Stark level of $^4S_{3/2}$, 725 $cm^{-1}$, is greater than the energy separation, 505 $cm^{-1}$, between the lowest and highest Stark level in the ground state $^4I_{15/2}$. Therefore, we assume that the ground state Stark levels thermalize much more rapidly than any radiative process and the population fractions of $Er^{3+}$ ions in the individual Stark levels of $^4I_{15/2}$ are proportional to the probabilities, $P_i(T)$, given by a Boltzmann distribution. The same is true for the Stark levels of the thermally coupled states $^2H_{11/2}$ and $^4S_{3/2}$. The relevant definitions for $P_i(T)$ are given in Supplementary Note 1.

The rate of laser-driven excitation from a ground state to an excited state takes the general form of:

$$W_{\mathrm{exc}} = \frac{\sigma I}{h\nu} N_{\mathrm{g}}, \tag{2}$$

where $N_g$ is the ground state population, $\sigma$ is the excitation cross section, $I$ is the laser intensity (in W $cm^{-2}$) and $h\nu$ is the photon energy of the incident light. The temperature dependence of $W_{\mathrm{exc}}(T)$ originates from the thermalization of the ground state Stark levels, $Z_i$, discussed above and the temperature dependence of the Stokes/anti-Stokes cross sections $\sigma(T)$. For the case of single-phonon-assisted Stokes and anti-Stokes transitions, these cross sections[11,25] are

$$\sigma_{ijl,\mathrm{S}}(T) = S_0 g_{\mathrm{p}} \sigma_{ij,\mathrm{res}} f_{\mathrm{bw},l} \left(1 - \mathrm{e}^{-\frac{\epsilon_l}{kT}}\right)^{-1}, \tag{3}$$

$$\sigma_{ijl,\mathrm{AS}}(T) = S_0 g_{\mathrm{p}} \sigma_{ij,\mathrm{res}} f_{\mathrm{bw},l} \left(\mathrm{e}^{\frac{\epsilon_l}{kT}} - 1\right)^{-1}, \tag{4}$$

where $\epsilon_l$ is the phonon energy, $S_0$ is the Pekar–Huang–Rhys coupling constant[25], $g_p$ is the degeneracy of the phonon mode and $\sigma_{ij,\mathrm{res}}$ is the resonance cross-section of the transition between subscripted levels. The derivation of $\sigma_{ij,\mathrm{res}}$ is described in the "Methods" section and given in Supplementary Table 1. The values of $\sigma_{ij,\mathrm{res}}$ determine the relative contribution of each individual Stark–Stark transition and are material-specific. In this expression for cross-section, we have introduced a factor $f_{\mathrm{bw},l}$, to account for the mismatch between $Er_2O_3$ phonon energies and the energy required to facilitate a phonon-assisted transition at the incident laser energy.

The term $f_{\mathrm{bw},l}$ is defined as

$$f_{\mathrm{bw},l} = \frac{L_l(\Delta_{ij}, \Gamma)}{L_l(\epsilon_l, \Gamma)}, \tag{5}$$

where $\Delta_{ij}$ is the difference between the incoming photon energy and the $i \rightarrow j$ Stark–Stark transition energy, $\epsilon_l$ is the center energy of the phonon, $\Gamma$ is the energy bandwidth (FWHM) of the phonon and $L_l(\epsilon, \Gamma)$ is a Lorentzian function centered at $\epsilon_l$ and defined as

$$L_l(\epsilon, \Gamma) = \frac{1}{\pi} \frac{\frac{1}{2}\Gamma}{(\epsilon - \epsilon_l)^2 + \left(\frac{1}{2}\Gamma\right)^2}. \tag{6}$$

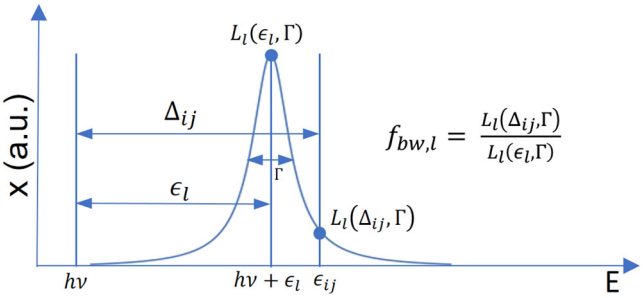


**Fig. 3 | A visual depiction of $f_{\mathrm{bw},l}$.** A schematic showing the difference between the incident photon energy ($h\nu$) and energy ($\epsilon_{ij}$) required for the i → j transition ($\Delta_{ij}$) relative to the finite bandwidth of a phonon centered at $\epsilon_l$ and how it relates to the bandwidth factor $f_{\mathrm{bw},l}$.

**Table 1 | Fit values for model parameters $R_{EF}$, Γ, and $S_0$ which are the ratio of Stark-state lifetimes, phonon bandwidth and Pekar–Huang–Rhys coupling constant, respectively**

| Parameter | Fit value |
|---|---|
| $R_{EF}$ | 1111 ± 68 |
| Γ | 1.86 ± 0.62 $cm^{-1}$ |
| $S_0$ ($^4S_{3/2}$) | 0.0046 ± 4e−4 |

Note that the uncertainties are due to the uncertainty of the fit and the uncertainty in the laser wavelength. Units are noted.

A schematic depicting $f_{\mathrm{bw},l}$ is given in Fig. 3 and the necessity of a finite phonon energy bandwidth is discussed in more detail in Supplementary Note 2 of the Supplemental Material. For the purposes of this study, we assume the same energy bandwidth for all phonon modes and that their energies and bandwidths do not vary significantly with temperature. The energy bandwidth for all the phonon modes, Γ, will be left as a fit parameter and reported in Table 1.

A value for the Pekar–Huang–Rhys coupling constant, $S_0$, is estimated from our data. The lack of any phonon replicas above the noise in our photoluminescence data constrains $S_0 \leq 0.01$ for these processes. Further, it has also been suggested that the electron–lattice coupling, and hence $S_0$ for the Stark levels of $^2H_{11/2}$ is stronger than that of $^4S_{3/2}$. To account for this, we allow for a different $S_0$ for Stark–Stark excitations involving $^2H_{11/2}$ compared to $^4S_{3/2}$ and take $S_0 = 0.01$ for Stark–Stark transitions involving $^2H_{11/2}$. We leave the $S_0$ for Stark–Stark transitions involving $^4S_{3/2}$ as a fit parameter and report it in Table 1. Note that $S_0 = 0.01$ is consistent with reported values for $Er^{3+}$ transitions in other materials[25].

Accounting for all possible laser-induced phonon-assisted Stark–Stark excitations between the ground state $^4I_{15/2}$ and the excited states $^2H_{11/2}$ and $^4S_{3/2}$, the total excitation rate out of the ground state may be expressed as

$$W_{\mathrm{exc}}(T) = \frac{I}{h\nu} N_{\mathrm{g}} \sum_{i=1}^{8} P_{Z_i}(T) \left( \sum_{l=0}^{48} \left( \sum_{j=1}^{6} \sigma_{Z_i,F_j,l}(T) + \sum_{k=1}^{2} \sigma_{Z_i,E_k,l}(T) \right) \right), \tag{7}$$

where $N_g$ is the total number of $Er^{3+}$ ions in the ground state $^4I_{15/2}$, $\sigma_{Z_i,F_j,l}(T)$ and $\sigma_{Z_i,E_k,l}(T)$ are the temperature-dependent phonon-assisted excitation cross sections using the phonon of energy $\epsilon_l$ for the $Z_i \rightarrow F_j$ transition and $Z_i \rightarrow E_k$ transition, respectively. The remaining variables were defined previously. Not all of the $\sigma_{ijl}(T)$ are expected to be non-zero; the total excitation rate is written this way for completeness. The value of $\Delta_{ij}$ sets the energy that material phonons have to match in order to facilitate a

transition. In order for a given Stark–Stark transition to occur, $\Delta_{ij}$ must fall within the finite energy Lorentzian envelope of a phonon mode in the host material otherwise $\sigma_{ijl}(T) \cong 0$. Using the measured $Er_2O_3$ phonon mode energies in the literature[30–36] and those calculated with density functional theory, and the finite bandwidth assumed above, we identified numerous possible Stokes and anti-Stokes single-phonon-assisted excitation processes at the measured laser wavelength of 532.03 ± 0.03 nm. The laser bandwidth is considered to be negligible (<3.3e−5 $cm^{-1}$) relative to the expected larger phonon bandwidths (typically several $cm^{-1}$).

An expression for the temperature-dependent lifetime of a given excited state Stark levels, $\tau_i(T)$, is found by noting that the population fractions of $Er^{3+}$ in $^2H_{11/2}$ and $^4S_{3/2}$ rapidly thermalize. That gives an $Er^{3+}$ ion in an excited Stark level numerous effective pathways to the ground state $^4I_{15/2}$. The total temperature-dependent lifetime for an $Er^{3+}$ ion in any individual Stark level in the excited state is a thermally weighted sum of these different pathways:

$$\frac{1}{\tau_i(T)} = \frac{\sum_n P_{F_n}(T)}{\tau_F} + \frac{\sum_n P_{E_n}(T)}{\tau_E} = \frac{\tau_E \sum_n P_{F_n}(T) + \tau_F \sum_n P_{E_n}(T)}{\tau_F \tau_E}, \quad (8)$$

where $P_{F_n}(T)$ and $P_{E_n}(T)$ have been defined previously. We define the lifetime of $Er^{3+}$ ions in an individual Stark level of $^4S_{3/2}$ as $\tau_E$ and $\tau_F$ for $^2H_{11/2}$. Those are the lifetime of $Er^{3+}$ ions exiting the combined excited state manifold of $^4S_{3/2}$ and $^2H_{11/2}$ from that individual Stark state, respectively. Those lifetimes would be the measured lifetime of the level in the absence of thermal coupling to the rest of the excited state Stark levels and are assumed to be temperature-independent.

Combining the expressions given above, the temperature-dependent population fraction, $N_i(T)$, of an $Er^{3+}$ ion in an excited state is given by

$$N_i(T) = A \sum_{m=1}^{8} P_m(T) \left( \sum_{l=0}^{48} \left( \sum_{j=1}^{6} \sigma_{Z_m,F_j,\omega_l}(T) + \sum_{k=1}^{2} \sigma_{Z_m,E_k,\omega_l}(T) \right) \right) P_i(T) \frac{1}{\tau_E \sum_n P_{F_n}(T) + \tau_F \sum_n P_{E_n}(T)}, \quad (9)$$

where $A$ is a constant combining all the temperature-independent constants and all other variables that have been defined previously. Given that $N_i$ is the dominant driver of the temperature dependence of the photoluminescence, the expression in Eq. (9) can be normalized and compared to the observed normalized photoluminescence arising from Stark-Stark radiative decays of each $E_i$ and $F_i$ Stark state.

## Discussion

There are four fitting parameters in Eq. (9), the lifetimes $\tau_F$ and $\tau_E$ of the Stark states in $^2H_{11/2}$ and $^4S_{3/2}$, respectively, the phonon energy bandwidth, Γ and the Pekar–Huang–Rhys constant, $S_0$, for the Stark–Stark transitions involving $^4S_{3/2}$. In what follows we will discuss how each parameter affects the model output, the fitting values we find from our data, and any conclusions we can draw from those values. The least squares fitting is done on only the normalized temperature-dependent photoluminescence arising from $E_1$. This is because the parameters are interrelated, the effect of variations in each parameter is seen in different temperature ranges and $E_1$ is the only level with non-zero emission over the entire temperature range. Regardless, good agreement with the data from $E_1$ yields good agreement with the data from $E_2$ and $F_{1-6}$.

Beginning with the lifetimes $\tau_E$ and $\tau_F$, we find that the predicted temperature for the peak of the normalized temperature-dependent photoluminescence from the Stark levels of the $^4S_{3/2}$ state, $E_1$ and $E_2$, depends only on the ratio $\frac{\tau_E}{\tau_F}$, which we will call $R_{EF}$. We also found that the normalized temperature-dependent behavior of all photoluminescence originating from Stark levels of the $^2H_{11/2}$, called $F_{1-6}$, is fairly insensitive to $R_{EF}$, compared to $E_1$ and $E_2$ (Supplementary Note 3).

Using our data, we can extract both the ratio of the lifetimes, $R_{EF}$, and the ratio of the radiative lifetimes, $R_{EF,rad} = \frac{\tau_{E,rad}}{\tau_{F,rad}}$. Fitting Eq. (9) to the normalized temperature-dependent data, we find that $R_{EF} = 1111$. We obtain $R_{EF,rad} = 8.6$ from the observed absolute photoluminescence signal. Given that $R_{EF}$ includes both radiative and nonradiative decay to the ground state and that $R_{EF} = 1111$, we conclude that $Er^{3+}$ ions in the $^2H_{11/2}$ levels decay non-radiatively at a much faster rate than do $Er^{3+}$ ions in the $^4S_{3/2}$ levels. This is consistent with a finding by M. Dammak et al.[37] that showed that the $^2H_{11/2}$ levels have a stronger electron–lattice coupling than the $^4S_{3/2}$ levels which would lead to an enhanced phonon-assisted rate of decay for $Er^{3+}$ in the $^2H_{11/2}$ levels. It is important to note that the concentration of $Er^{3+}$ ions in $Er_2O_3$ is 2e22 ions $cm^{-3}$, well above 1e20 ions $cm^{-3}$ which is the threshold where non-radiative energy transfer processes between ions are observed to become relevant for radiative emission in Er-doped materials[38]. Therefore, the lifetime ratio found here will differ from those found in more dilute Er-doped samples. Furthermore, the form of Eq. (8) assumes that the intrinsic lifetimes, $\tau_E$ and $\tau_F$, are temperature independent. It is not clear if this is true, but determining that is beyond the scope of this paper.

The effect of variations in the phonon energy bandwidth, Γ, and the Pekar–Huang–Rhys constant, $S_0$, for excitation to $^4S_{3/2}$ is discernible only in the low-temperature behavior (<100 K) of the photoluminescence arising from the $E_1$ Stark level of $^4S_{3/2}$; the other levels, $E_2$ and $F_{1-6}$, show minimal variation as a function of either parameter. The predicted low-temperature photoluminescence arising from $E_1$ increases when either Γ or $S_0$ is increased. We find that $\Gamma = 1.86\ cm^{-1}$ and $S_0 = 0.0046$ for Stark–Stark transitions involving $^4S_{3/2}$ gives the best agreement with observation. Once again, the reduction of $S_0$ for the $^4S_{3/2}$ relative to $^2H_{11/2}$ is consistent with the finding by M. Dammak et al.[37]. Figure 4 shows the final result of the fitting.

Conceptually, the temperature dependence of the emitted luminescence from a given excited state Stark level can be understood in the following way. At all temperatures, $Er^{3+}$ ions excited by Stokes/anti-Stokes excitation rapidly thermalize between the excited state Stark levels of $^4S_{3/2}$ and $^2H_{11/2}$ prior to any decay to the ground state $^4I_{15/2}$. This means that at temperatures below 30 K, $Er^{3+}$ ions only populate the $E_1$ level, and only photoluminescence arising from decays of $E_1$ is observed. Above 30 K, $Er^{3+}$ ions begin to populate the $E_2$ level, and photoluminescence arising from decays from that level is observed as well. Once the temperature increases above 100 K, $Er^{3+}$ ions more readily populate the $^2H_{11/2}$ (F) levels, and emission is observed from those as well.

The increase in emission with temperature from all levels is because the excitation rate, $W_{exc}(T)$, increases with increasing temperature. For the $^2H_{11/2}$ (F) levels, this increase is evident at all temperatures once thermal excitation begins to populate those levels. For the $^4S_{3/2}$ (E) levels, this increase is only evident below 140 K. This is because the lifetime of $Er^{3+}$ ions in the Stark levels of $^2H_{11/2}$, $\tau_F$, is significantly shorter than the lifetime of $Er^{3+}$ ions in the Stark levels of $^4S_{3/2}$, $\tau_E$. As the temperature increases above 100 K, the $^4S_{3/2}$ levels begin to be emptied via thermal excitation and subsequent decay through the $^2H_{11/2}$ levels. Around 140 K, the effect of the increasing excitation rate on the $^4S_{3/2}$ photoluminescence is overtaken by the quenching effect of thermal excitation to the $^2H_{11/2}$ levels and the photoluminescence from $^4S_{3/2}$ begins to decrease.

It is important to note that the existence of a photoluminescence signal at temperatures below 50 K is exclusively governed by Stokes excitation. The omission of Stokes excitation pathways leads to a significant deviation from our observations for $E_1$ and $E_2$ below 75 K. In order to incorporate any Stokes excitation pathway and predict photoluminescence below 50 K, multiple anti-Stokes excitation pathways are also required to accurately describe our observations at elevated temperatures. Above 75 K, without the inclusion of multiple Stokes and anti-Stokes excitation pathways in Eq. (7), the temperature dependence of our observed photoluminescence signal over the entire temperature range cannot be accurately described.

In conclusion, we can account for the temperature dependence of the photoluminescence from 4 to 300 K arising from the $^2H_{11/2} \rightarrow {}^4I_{15/2}$, $^4S_{3/2} \rightarrow {}^4I_{15/2}$, and $^4S_{3/2} \rightarrow {}^4I_{13/2}$ transitions of $Er^{3+}$ in $Er_2O_3$ induced by

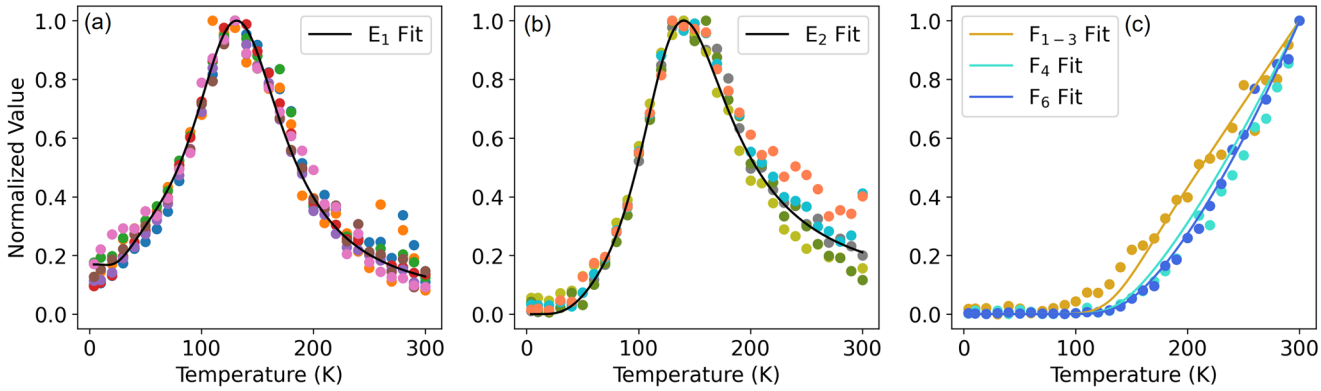


**Fig. 4 | Model fits to the normalized measured photoluminescence from $Er^{3+}$ in $Er_2O_3$. a–c** Model fit to the observed normalized photoluminescence originating from $Er^{3+}$ decaying from the $E_1$ and $E_2$ levels of $^4S_{3/2}$ and the $F_{1-3}$, $F_4$, and $F_6$ levels of $^2H_{11/2}$.

phonon-assisted Stark–Stark excitations. We comprehensively treat the individual Stark-split states and consider the multiple single-phonon-assisted excitations between them which are permitted by the material-specific phonons at the incident laser wavelength. Without these considerations, it would not be possible to fully account for the measured data, particularly below 75 K. This model demonstrates how the phononic interactions of $Er^{3+}$ with the host lattice lead to the observed temperature-dependent behavior of the photoluminescence and predicts expected variations in that behavior due to changes in the incident excitation wavelength.

Fitting the model yields a lifetime ratio $R_{EF}$ that leads us to conclude that $Er^{3+}$ ions in the $^2H_{11/2}$ levels decay non-radiatively more rapidly than $Er^{3+}$ in the $^4S_{3/2}$ levels. That combined with the derived value of $S_0$ for phonon-assisted transition involving the Stark-split levels of $^4S_{3/2}$ gives additional evidence that the electron–phonon coupling is stronger for the $^2H_{11/2}$ states than the $^4S_{3/2}$ states. Additionally, this model suggests that variations in the wavelength of the excitation source ( ~ 0.1 nm) may significantly influence the temperature dependence of emission from $Er^{3+}$ (Supplementary Note 3), an avenue that has only recently begun to be explored[29].

The study of these transitions in the near-ideal configuration of an $Er_2O_3$ single crystal provides insights into the role of the phonons in determining the $Er^{3+}$ optical emission. This approach provides a base to explore critical aspects of Er-based systems such as the role of defects and their subsequent modification of the Stark-split levels and perturbation of the local phonon modes. Our findings and proposed explanations not only contribute to the understanding of the complex interactions of $Er^{3+}$ with this crystalline host but also pave the way for future studies of $Er^{3+}$ in wide bandgap semiconductors such as SiC and $Ga_2O_3$.

## Methods

### Sample growth and characterization

We examined a nominally 100 nm-thick $Er_2O_3$ film epitaxially grown on a Si(111) substrate by molecular beam epitaxy (MBE). The Si(111) wafer was degreased in acetone, methanol, and deionized water with sonication before loading into the MBE deposition system. After outgassing the wafer at 650 °C, the native oxide was desorbed by flashing to 850 °C for 15 min. In order to protect the Si from oxidation during $Er_2O_3$ deposition, a one-third monolayer of Sr metal was deposited at 600 °C resulting in a $3 \times 3$ surface reconstruction of the Si(111) surface. For $Er_2O_3$ deposition, Er metal from an effusion cell and molecular oxygen were introduced into the deposition chamber. The Er effusion cell was operated at 1195 °C resulting in an Er metal flux of 4 A per minute. Molecular oxygen was first allowed to flow until the total pressure was $2 \times 10^{-7}$ Torr. Once this pressure has been achieved, the Er shutter is opened while the substrate temperature is quickly ramped from 600 to 700 °C, with oxygen pressure increasing until it reached $2 \times 10^{-6}$ Torr. These conditions were then maintained until the desired thickness was achieved, after which the main shutter was closed, and the substrate cooled at 30 °C/min to room temperature in oxygen.

Supplementary Fig. 2a shows the reflection high-energy electron diffraction (RHEED) pattern of the $Er_2O_3$ film immediately after growth indicating a well-ordered, flat surface. After unloading from the MBE chamber, x-ray diffraction was used to measure the lattice constant and overall crystallinity, and x-ray reflectivity was used to measure thickness. Supplementary Fig. 2b shows the $Er_2O_3$ 222 region indicating a high level of crystallinity consistent with a strained single-crystal of C-type bixbyite structure. In-situ RHEED during growth indicates that $Er_2O_3$ initially grows tensile strained to Si and gradually relaxes to its bulk lattice constant (peak shift to lower angle) with increased thickness. No other orientations or phases were found in the wide-angle x-ray diffraction scan. X-ray reflectivity reveals the actual $Er_2O_3$ film thickness to be 93.5 nm. Rutherford backscattering spectrometer (RBS) with a 2 MeV He ion beam, shown in Supplementary Fig. 3, confirmed this film thickness and further determined that the film is stoichiometric of $Er_2O_3$ within the measurement uncertainties of ~ 3%.

### Temperature-dependent photoluminescence

Temperature-dependent photoluminescence was acquired using a home-built confocal microscope in a Montana Instruments CryoStation equipped with a Zeiss LD EC Epiplan- Neofluar ×100 DIC M27 objective (0.85NA) described in further detail in other publications[39–42]. This setup enabled precise temperature regulation within the range of 4–300 K. A Cobolt Samba 532 nm laser, measured to be 532.03 ± 0.03 nm with a bandwidth <1 MHz (<3.3e−5 $cm^{-1}$), was utilized as the CW excitation source. Photoluminescence spectra were acquired with an IsoPlane SCT 320 spectrometer with a 600 and 2400 lines $mm^{-1}$ grating and a Pixis 400BR eXcelon camera. Bragg filters were used to acquire spectra within 10 $cm^{-1}$ of the laser line, including a Bragg dichroic beamsplitter and two Bragg filters in the collection optics with associated irises used to suppress residual laser light. A schematic of the optics train is shown in the supplemental information (Supplementary Fig. 4).

The temperature-dependent photoluminescence data was collected in the following manner. The Montana CryoStation was cooled to 4 K with the sample mounted inside. Cooling the closed loop takes several hours. Once the temperature stabilized, the laser was focused on the surface of the sample. This was confirmed by using a beam splitter to redirect some intensity onto a camera (Supplementary Fig. 4). This beam splitter is on a motorized mount and is removed during data collection. Photoluminescence data was then collected. After completing the data collection at a given temperature the focus was checked to ensure stability through the duration of the measurement. Measurements were repeated in the rare event that the focus drifted. The sample was then warmed to the next temperature (10 K) and the process described above was repeated. This process was continued at increments of 10 K (20, 30 K, etc.) up to 300 K and was

conducted at several different points on the sample to ensure the reliability of the data.

The integrated photoluminescence given in Fig. 1c was calculated by integrating over the full transition manifold. For the $^4S_{3/2} \rightarrow {}^4I_{15/2}$ manifold, Si Raman lines, located at 547.7 nm and near 561 nm had to be removed. In our data, the Raman line near 547.7 nm was found to not be easily characterized by a Lorentzian lineshape and had to be removed by excluding the wavelength range from 547 to 548.2 nm from the integration. This omitted the $E_2 \rightarrow Z_2$ transition from the integrated total and based on Supplementary Table 1, this introduced an error of ~1–3% to the integrated photoluminescence value. The second-order Raman peak was removed by noting that its contribution was roughly constant with temperature. At 4 K, there are no $Er^{3+}$ lines co-located with the Raman peak. Therefore, we integrated the 4 K data from 560 to 562.7 nm and removed that value from the integrated total at each temperature. The normalized intensities displayed in Fig. 2b and c were found by fitting each observed spectral line to a Lorentzian line shape at each temperature. In the case of overlapping, but still resolved spectral lines, a sum of Lorentzian lines was employed. The fit values for the peak heights were then normalized to the maximum value observed for that peak over the full temperature range.

### Stark–stark resonance cross-sections

Using the method outlined in Aull et al.[43], and given below in Eq. (10), we derived the cross sections. Note that the spectral variations of the host refractive index are negligible over the wavelength region for these transitions.

$$\frac{I_{ji}(\nu)}{I_{j'i'}(\nu)} = \left(\frac{\nu}{\nu'}\right)^3 \frac{N_j}{N_{j'}} \frac{\sigma_{ji}(\nu)}{\sigma_{j'i'}(\nu')}, \tag{10}$$

where $I_{ji}$ is the fluorescent intensity of the $j \rightarrow i$ transition, $\nu$ is the frequency of the emitted light, $N_j$ is the population density of $j$ and $\sigma_{ji}(\nu)$ is the emission cross section for the $j \rightarrow i$ transition. The emission and absorption cross-sections are related by

$$\sigma_{ji}(\nu) = \left(\frac{g_i}{g_j}\right)\sigma_{ij}(\nu), \tag{11}$$

where $\sigma_{ij}(\nu)$ is the absorption cross section for $i \rightarrow j$ and $g_i$ and $g_j$ are the degeneracies of $i$ and $j$, respectively. All of the Stark-split levels are doubly degenerate[44] so for our case the absorption and emission cross sections are equal.

We obtain the peak heights by fitting the spectra shown in Supplementary Fig. 1 with Lorentzian distributions centered at the wavelengths calculated using the energy levels reported by Gruber et al.[44]. These spectra were taken at temperatures that maximized the observed photoluminescence from these transitions. Our instrument had a uniform shift of 0.2 nm relative to the calculated wavelengths. That shift is attributed to a systematic calibration error. The peak heights of those Lorentzian distributions resulting from the fits to Supplementary Fig. 1 are used as $I_{ji}(\nu)$.

Using the extracted values of $I_{ji}(\nu)$, we use the $Z_1 \rightarrow$ Excited level (for instance $E_1$) cross section from Gruber et al.[28] to obtain the remainder of the $Z_i \rightarrow E_1$ cross sections. This process is followed for the remaining excited Stark-split states. This approach simplifies the application of Eq. (10) because in each case $j = j'$ meaning that $\frac{N_j}{N_{j'}} = 1$. The cross sections relevant to the model are listed in the second column of Supplementary Table 1 next to the relevant Stark–Stark transition.

### Phonon energies

Phonon mode frequencies and their irreducible representations were calculated using the Phonopy[45,46] package with forces calculated using density functional theory (DFT) as implemented in the VASP[47] software package. Harmonic phonons were calculated employing a central finite difference scheme with an ionic displacement of ±0.01 Å for each atom. For the density-functional-theory calculations, the valence–core interaction was described using PAW pseudopotentials[48,49] with the standard oxygen potential ($2s^2 2p^4$ valency) and the $Er^{3+}$ potential ($5p^6 6s^2 5d^1$ valency with $4f^{11}$ frozen in core). The plane-wave basis cutoff was set to 800 eV. The exchange-correlation interaction was described using the generalized gradient approximation (GGA) as originally parameterized by Perdew, Burke, and Ernzerhof and revised for solids (PBEsol)[50]. For initial structure optimization, the Brillouin zone integration was done using a $4 \times 4 \times 4$ Monkhorst–Pack $k$-point grid[51]. For phonon calculations, a $2 \times 2 \times 2$ supercell was utilized and the $k$-point grid was reduced accordingly. The optimized lattice constants are 10.416 Å with good agreement compared to the experimental value[52–54]. We compare the calculated phonon mode frequencies to previous experiments (Supplementary Table 2) and find good overall agreement[30–36]. Not all modes have been observed experimentally as some, for example, are hyper-Raman modes (i.e., silent modes).

Combining the DFT calculations and experimental observations ranging from 4 to 300 K, phonon energies in $Er_2O_3$ shift by ~3-4 $cm^{-1}$ uniformly to lower energies[31,33,35], with much of the shift being observed to occur above 80 K[33]. Studies in $Lu_2O_3$, which like $Er_2O_3$ is a rare-earth sesquioxide with C-type bixbyite crystal structure, show that at least in the case of one phonon mode, much of the observed energy shift and broadening of the energy of the phonon mode occurs above 200 K[55]. The transition energies between Stark-split levels of $Er^{3+}$ in $Er_2O_3$ also shift with temperature by ~3 $cm^{-1}$ to lower energies[19,56]. Given that both the $Er^{3+}$ transition energies and the phonon energies shift nearly identically to lower energies, and that much of the shift is expected to occur above 200 K, we will take both to be constant over the measured temperature range and adopt the values reported near 10 K.

The column entitled 'assumed value' in Supplementary Table 2 is the energy of the phonon mode used in the model. To arrive at this assumed value, if no experimental measurement had been made, we took the theoretical value, and rounded to the nearest 0.1 $cm^{-1}$. The theoretical value is calculated at 0 K. For those modes where an experimental value was known, we averaged over the low-temperature experimental values, rounded to the nearest 0.1 $cm^{-1}$. Almost all of the experimental values for the phonon energies span a 1–2 $cm^{-1}$ range, leading to minimal uncertainty in the averaged value of the phonon energy used in the model. However, for some phonon modes, the experimental values span a range of up to 10 $cm^{-1}$.

To demonstrate the effect of that uncertainty, we take the $T_g$ mode (theoretical value 390.4 $cm^{-1}$) and plot the output of our model while varying the energy of this mode between the lower bound and upper bounds, 380 and 390 $cm^{-1}$, respectively. This is plotted in Supplementary Fig. 6. From this figure, it is clear that there is minimal variation in the model output as the assumed phonon energy of that $T_g$ mode is varied. Given the minimal variation in model output, as this mode energy varies over the range of 380–390 $cm^{-1}$, it is reasonable to assume that the variation is negligible for any individual phonon mode with smaller uncertainty in the mode energy. For that reason, we simply average the experimental values near 10 K and take those values for our model.

### Calculating $R_{EF,rad}$

Using Eq. (1), we can find a rough estimate $R_{EF,rad}$. Note that $A_i = \frac{1}{\tau_{i,r}}$, therefore, $R_{EF,rad} = \frac{A_E}{A_E}$. Returning to Eq. (1) and invoking Eqs. (S2) and (S3), this means that:

$$R_{EF,rad} = \frac{I_F \sum P_E(T)}{I_E \sum P_F(T)}, \tag{12}$$

where $I_F$ is the integrated intensity of the F lines, $I_E$ is the integrated intensity of the E lines. Using our measured data, we found this value at all temperatures where photoluminescence could be readily observed from the F lines (>200 K) and the average of that value is 8.6 and decreases slowly with increasing temperature.

## Data availability

The data that support the findings of this study are available from the corresponding author upon reasonable request.

Received: 28 October 2023; Accepted: 12 February 2024;
Published online: 28 February 2024

## References

1. Thiel, C. W., Bottger, T. & Cone, R. L. Rare-earth-doped materials for applications in quantum information storage and signal processing. *J. Lumin.* **131**, 353–361 (2011).
2. Pak, D. et al. Long-range cooperative resonances in rare-earth ion arrays inside photonic resonators. *Commun. Phys*. **5**, 89 (2022).
3. Awschalom, D. D., Hanson, R., Wrachtrup, J. & Zhou, B. B. Quantum technologies with optically interfaced solid-state spins. *Nat. Photonics* **12**, 516–527 (2018).
4. Raha, M. et al. Optical quantum nondemolition measurement of a single rare earth ion qubit. *Nat. Commun.* **11**, 1–7 (2020).
5. Judd, B. R. Optical absorption intensities of rare-earth ions. *Phys. Rev.* **127**, 750–761 (1962).
6. Ofelt, G. S. Intensities of crystal spectra of rare-earth ions. *J. Chem. Phys.* **37**, 511–520 (1962).
7. Zhanci, Y., Shihua, H., Shaozhe, L. & Baojiu, C. Radiative transition quantum efficiency of $^2H_{11/2}$ and $^4S_{3/2}$ states of trivalent erbium ion in oxyfluoride tellurite glass. *J. Non. Cryst. Solids* **343**, 154–158 (2004).
8. Lou, H. et al. Temperature-dependent photoluminescence spectra of Er–Tm-codoped $Al_2O_3$ thin film. *Appl. Surf. Sci.* **255**, 8217–8220 (2009).
9. Wang, S. et al. Temperature dependence of luminescence behavior in $Er^{3+}$-doped $BaY_2F_8$ single crystal. *Phys. B Condens. Matter* **431**, 37–43 (2013).
10. Capobianco, J. A., Vetrone, F., Boyer, J. C., Speghini, A. & Bettinelli, M. Visible upconversion of $Er^{3+}$ doped nanocrystalline and bulk $Lu_2O_3$. *Opt. Mater.* **19**, 259–268 (2002).
11. Da Silva, C. J. & De Araujo, M. T. Thermal effect on upconversion fluorescence emission in $Er^{3+}$-doped chalcogenide glasses under anti-stokes, stokes and resonant excitation. *Opt. Mater.* **22**, 275–282 (2003).
12. Bhiri, N. M. et al. Stokes and anti-Stokes operating conditions dependent luminescence thermometric performance of $Er^{3+}$-doped and $Er^{3+}$, $Yb^{3+}$ co-doped $GdVO_4$ microparticles in the non-saturation regime. *J. Alloys Compd*. **814**, 152197 (2020).
13. Koepke, C., Wisniewski, K. & Środa, M. Primary- and upconverted emission in the glass and glass-ceramics doped with $Er^{3+}$ ions in the context of maximum phonons. *J. Alloys Compd*. **883**, 160785 (2021).
14. Omi, H., Tawara, T. & Tateishi, M. Real-time synchrotron radiation X-ray diffraction and abnormal temperature dependence of photoluminescence from erbium silicates on $SiO_2$/Si substrates. *AIP Adv.* **2**, 012141 (2012).
15. Dos Santos, P. V. et al. Thermally induced threefold upconversion emission enhancement in nonresonant excited $Er^{3+}$/$Yb^{3+}$-codoped chalcogenide glass. *Appl. Phys. Lett.* **74**, 3607–3609 (1999).
16. Adachi, S., Kawakami, Y., Kaji, R., Tawara, T. & Omi, H. Energy transfers in telecommunication-band region of $(Sc,Er)_2O_3$ thin films grown on Si(111). *J. Phys. Conf. Ser*. **647**, 012031 (2015).
17. Adachi, S., Kawakami, Y., Kaji, R., Tawara, T. & Omi, H. Investigation of population dynamics in 1.54-μm telecom transitions of epitaxial $(Er_xSc_{1-x})_2O_3$ thin layers for coherent population manipulation: weak excitation regime. *Appl. Sci.* **8**, 1–13 (2018).
18. Monemar, B. & Titze, H. Infrared excitation of visible $Er^{3+}$-luminescence in $Yb^{3+}$-sensitized $YF_3$. *Phys. Scr.* **4**, 83–88 (1971).
19. Choi, H., Shin, Y. H. & Kim, Y. Temperature dependence of the Stark shifts of $Er^{3+}$ transitions in $Er_2O_3$ thin films on Si(001). *J. Korean Phys. Soc.* **76**, 1092–1095 (2020).
20. Kisliuk, P., Krupke, W. F. & Gruber, J. B. Excited-state dynamics of $Er^{3+}$ in $Gd_2O_3$ nanocrystals. *J. Phys. Chem. C* **111**, 9638–9643 (2007).
21. Omi, H. & Tawara, T. Energy transfers between $Er^{3+}$ ions located at the two crystalographic sites of $Er_2O_3$ grown on Si(111). *Jpn. J. Appl. Phys.* **51**, 2–5 (2012).
22. Da Silva, C. J., De Araujo, M. T., Gouveia, E. A. & Gouveia-Neto, A. S. Thermal effect on multiphonon-assisted anti-Stokes excited upconversion fluorescence emission in $Yb^{3+}$-sensitized $Er^{3+}$-doped optical fiber. *Appl. Phys. B Lasers Opt.* **70**, 185–188 (2000).
23. Saha, S. et al. Anomalous temperature dependence of phonons and photoluminescence bands in pyrochlore $Er_2Ti_2O_7$: signatures of structural deformation at 130 K. *J. Phys. Condens. Matter* **23**, 445402 (2011).
24. Kuznetsov, A. S., Sadofev, S., Schäfer, P., Kalusniak, S. & Henneberger, F. Single crystalline $Er_2O_3$:sapphire films as potentially high-gain amplifiers at telecommunication wavelength. *Appl. Phys. Lett.* **105**, 191111 (2014).
25. Auzel, F. Multiphonon-assisted anti-Stokes and Stokes fluorescence of triply ionized rare-earth ions. *Phys. Rev. B* **13**, 2809–2817 (1976).
26. Yokokawa, T., Inokuma, H., Ohki, Y., Nishikawa, H. & Hama, Y. Nature of photoluminescence involving transitions from the ground to $4f^{n-1}$ $5d^1$ states in rare-earth-doped glasses. *J. Appl. Phys.* **77**, 4013–4017 (1995).
27. Gruber, J. B., Henderson, J. & Muramoto, M. Energy levels of single-crystal erbium. *J. Chem. Phys.* **45**, 477–482 (1966).
28. Gruber, J. B., Burdick, G. W., Chandra, S. & Sardar, D. K. Analyses of the ultraviolet spectra of $Er^{3+}$ in $Er_2O_3$ and $Er^{3+}$ in $Y_2O_3$. *J. Appl. Phys.* **108**, 023109 (2010).
29. De, A. et al. Resonance/off-resonance excitations: implications on the thermal evolution of $Eu^{3+}$ photoluminescence. *J. Mater. Chem. C* **11**, 6095–6106 (2023).
30. Dilawar, N. et al. A Raman spectroscopic study of C-type rare earth sesquioxides. *Mater. Charact.* **59**, 462–467 (2008).
31. Schaack, G. & Koningstein, J. A. Phonon and electronic Raman spectra of cubic rare-earth oxides and isomorphous yttrium oxide*. *J. Opt. Soc. Am.* **60**, 1110 (1970).
32. Wang, J. C. & Zhu, Y. Y. Study on the structural properties of polycrystalline $Er_2O_3$ films on Si(001) substrates by Raman spectra. *Adv. Mater. Res.* **953–954**, 1091–1094 (2014).
33. Gruber, J. B., Chirico, R. D. & Westrum, E. F. Jr. Correlation of spectral and heat-capacity Schottky contributions for $Dy_2O_3$, $Er_2O_3$, and $Yb_2O_3$. *J. Chem. Phys.* **76**, 4600–4605 (1982).
34. Yan, D. et al. Assignments of the Raman modes of monoclinic erbium oxide. *J. Appl. Phys.* **114**, 193502 (2013).
35. Bloor, D. & Dean, J. R. Spectroscopy of rare earth oxide systems. I. Far infrared spectra of the rare earth sesquioxides, cerium dioxide and nonstoichiometric praseodymium and terbium oxides. *J. Phys. C Solid State Phys.* **5**, 1237–1252 (1972).
36. Lejus, A. M. & Michel, D. Raman spectrum of $Er_2O_3$ sesquioxide. *Phys. Stat. Sol.* **84**, K105–K108 (1977).
37. Dammak, M. & Zhang, D. Spectra and energy levels of $Er^{3+}$ in $Er_2O_3$ powder. *J. Alloys Compd.* **407**, 8–15 (2006).
38. Polman, A. Erbium implanted thin film photonic materials. *J. Appl. Phys.* **82**, 1–39 (1997).
39. Pai, Y. Y. et al. Mesoscale interplay between phonons and crystal electric field excitations in quantum spin liquid candidate $CsYbSe_2$. *J. Mater. Chem. C* **10**, 4148–4156 (2022).
40. Pai, Y. Y. et al. Magnetostriction of α-$RuCl_3$ flakes in the zigzag phase. *J. Phys. Chem. C* **125**, 25687–25694 (2021).
41. Luo, W. et al. Improving strain-localized GaSe single photon emitters with electrical doping. *Nano Lett.* **23**, 9740–9747 (2023).
42. Li, H. et al. Observation of unconventional charge density wave without acoustic phonon anomaly in kagome superconductors A V3Sb5 (A = Rb, Cs). *Phys. Rev. X* **11**, 1–9 (2021).

43. Aull, B. F. & Jenssen, H. P. Vibronic interactions in Nd:YAG resulting in nonreciprocity of absorption and stimulated emission cross sections. *IEEE J. Quantum Electron.* **18**, 925–930 (1982).
44. Kisliuk, P., Krupke, W. F. & Gruber, J. B. Spectrum of $Er^{3+}$ in single crystals of $Y_2O_3$. *J. Chem. Phys.* **40**, 3606–3610 (1964).
45. Togo, A. & Tanaka, I. First principles phonon calculations in materials science. *Scr. Mater.* **108**, 1–5 (2015).
46. Togo, A. First-principles phonon calculations with phonopy and phono3py. *J. Phys. Soc. Japan* **92**, 1–21 (2023).
47. Kresse, G. & Furthmüller, J. Efficient iterative schemes for ab initio total-energy calculations using a plane-wave basis set. *Phys. Rev. B—Condens. Matter Mater. Phys.* **54**, 11169–11186 (1996).
48. Kresse, G. & Joubert, D. From ultrasoft pseudopotentials to the projector augmented-wave method. *Phys. Rev. B—Condens. Matter Mater. Phys.* **59**, 1758–1775 (1999).
49. Blöchl, P. E. Projector augmented-wave method. *Phys. Rev. B* **50**, 17953–17979 (1994).
50. Perdew, J. P. et al. Restoring the density-gradient expansion for exchange in solids and surfaces. *Phys. Rev. Lett.* **100**, 1–4 (2008).
51. Monkhorst, H. J. & Pack, J. D. Special points for Brillonin-zone integrations*. *Phys. Rev. B* **16**, 1748–1749 (1977).
52. Eyring, L. R. Chapter 27 The binary rare earth oxides. *Handb. Phys. Chem. Rare Earths* **3**, 337–399 (1979).
53. Norton, D. P. Synthesis and properties of epitaxial electronic oxide thin-film materials. *Mater. Sci. Eng. R Rep.* **43**, 139–247 (2004).
54. Xu, R. et al. Epitaxial growth of $Er_2O_3$ films on Si(0 0 1). *J. Cryst. Growth* **277**, 496–501 (2005).
55. Bura, N., Yadav, D., Singh, J. & Sharma, N. D. Phonon variations in nano-crystalline lutetium sesquioxide under the influence of varying temperature and pressure. *J. Appl. Phys*. **126**, 245901 (2019).
56. Dean, J. R. & Bloor, D. Spectroscopy of rare earth oxide systems. II. Spectroscopic properties of erbium oxide (at antiferromagnetic transition). *J. Phys. C Solid State Phys.* **5**, 2921–2940 (1972).


## Acknowledgements

The work at Vanderbilt University was supported by funds from the School of Arts and Science and by the McMinn Endowment. The work at the University of Texas was supported by the Air Force Office of Scientific Research under grant FA9550-18-1-0053. Photoluminescence microscopy was supported by the Center for Nanophase Materials Sciences (CNMS2022-B-01577), a U.S. Department of Energy Office of Science User Facility. This work was performed, in part, at the Center for Integrated Nanotechnologies (CINT#2022AU0120), an Office of Science User Facility operated by the U.S. Department of Energy (DOE) Office of Science. Los Alamos National Laboratory, an affirmative action-equal opportunity employer, is managed by Triad National Security, LLC for the U.S. Department of Energy's NNSA, under contract 89233218CNA000001.

## Author contributions

A.D., H.W., and N.H.T. conceived the experiments. M.T. contributed to the conception of the experiments. A.D. and H.W. performed the experiments and analyzed the data. H.K. contributed to the data analysis of $Er^{3+}$ photoluminescence. A.D. lead the effort to develop the model with support from all co-authors. A.R. and A.B.P. grew and characterized the $Er_2O_3$ film on Si(111). S.A. conducted the theoretical phonon calculations. B.L. provided facilities and guidance for temperature-dependent measurements. Y.W. conducted RBS characterization of $Er_2O_3$ film. A.U. provided facilities and guidance for initial room temperature experiments. A.A.D. supported sample fabrication and theoretical phonon calculations. A.O. and S.T.P. supported theoretical parts. A.D. wrote the manuscript with feedback from all co-authors. All authors participated in discussions. The project was supervised by J.D., A.H., L.C.F. and N.H.T.

## Competing interests

The authors declare no competing interests.

## Additional information

**Supplementary information** The online version contains supplementary material available at https://doi.org/10.1038/s42005-024-01559-z.

**Correspondence** and requests for materials should be addressed to Adam Dodson.

**Peer review information** *Communications Physics* thanks Madhab Pokhrel, YunXin Liu and the other, anonymous, reviewer(s) for their contribution to the peer review of this work.